Reactions of Laser-Ablated Co, Rh, and Ir with CO: Infrared Spectra and Density Functional Calculations of the Metal Carbonyl Molecules, Cations and Anions in Solid Neon

Mingfei Zhou and Lester Andrews*

Department of Chemistry, University of Virginia, Charlottesville, Virginia 22901

Received: April 28, 1999; In Final Form: August 6, 1999

Laser ablation produces metal atoms, cations, and electrons for reaction with CO during condensation in excess neon at 4 K. Infrared spectra are observed for the metal carbonyls, cations, and anions, which are identified from isotopic shifts (^{13}CO, $C^{18}O$) and splittings using mixed isotopic precursors. Density functional calculations with pseudopotentials for Rh and Ir predict the observed carbonyl stretching frequencies within 1−2%. This characterization of the simple $RhCO^+$, RhCO, and $RhCO^-$ (and Ir) species over a 350 cm^{-1} range provides a scale for comparison of larger catalytically active Rh and Ir carbonyl complexes in solution and on surfaces to estimate charge on the metal center. This work provides the first spectroscopic characterization of Rh and Ir carbonyl cations and anions except for the stable tetracarbonyl anions in solution.

Introduction

Transition metal carbonyls are important reagents in organometallic chemistry, and cobalt, rhodium, and iridium carbonyls and complexes, in particular, are widely used as catalyst systems.[1,2] Coordinatively unsaturated metal carbonyls have been suggested as active catalyst sites in several processes, particularly for rhodium supported on alumina,[3,4] silica,[5] and zeolites,[6] where $Rh^I(CO)_2$ photodissociates to give the $Rh^I(CO)$ active species, and for $CpRh(CO)_2$, where a CpRh(CO) transient has been characterized.[7] Monocarbonyl absorptions have been observed at 2096, 2061, and 1985 cm^{-1} for active species[3b,4b,5c,7a] and in the 1950−2020 cm^{-1} region for a series of phosphine complexes.[8] The coordinatively unsaturated neutral $M(CO)_x$ radicals may provide a model for these intermediates, but with the addition of the corresponding cation and anion carbonyl species, a clear trend of carbonyl vibrational frequency dependence on metal charge can be determined.

Since rhodium metal is among the best catalysts for removal of carbon monoxide and nitric oxide from auto exhaust gases, it is important to characterize the adsorption of CO on the clean metal surface. Too many studies have been done for rhodium and iridium to reference here, but very recent infrared investigations of low monolayer coverage of linearly adsorbed CO are particularly relevant.[9,10]

Earlier thermal Co, Rh, and Ir atom matrix isolation investigations identified neutral $M(CO)_{1-4}$ species in solid argon.[11,12] In addition, laser-ablation experiments with cobalt formed the $M(CO)_{1-4}^-$ anions,[13] and the stable $Co(CO)_4^-$ anion gave the same infrared absorption as found in THF solution.[14] We report here reactions of laser-ablated Co, Rh, and Ir with CO in excess neon, which produce better resolved neutral species and in addition the first infrared spectra of group 9 metal carbonyl cation and anion species, except for the stable tetracarbonyl anions in solution,[15,16] which are in agreement. Matrix infrared observation of the simple $MCO^{+,0,-}$ monocarbonyl series provides a scale by which a metal charge in larger complex ions and supported catalysts sites can be estimated.

Finally, the Rh and Ir carbonyl spectra including cations and anions provide a database to test density functional theory (DFT) vibrational frequency calculations using pseudopotentials for comparison with experimental results. The RhCO species have been calculated previously by DFT and post-Hartree−Fock methods.[17−21] We report here excellent (1−2%) agreement between observed neon matrix and DFT calculated frequencies for Rh and Ir carbonyl neutral, cation, and anion systems.

Experimental Section

The experiment for laser ablation and matrix isolation spectroscopy has been described in detail previously.[22−24] Briefly, the Nd:YAG laser fundamental (1064 nm, 10 Hz repetition rate, 10 ns pulse width) was focused on the rotating metal target (Goodfellow Metals) using low energy (1−5 mJ/pulse). Laser-ablated metal atoms were co-deposited with carbon monoxide (0.1, 0.2, 0.5%) in neon onto a 4 K CsI cryogenic window at 2−4 mmol/h for 30−60 min. Carbon monoxide (Matheson), isotopic $^{13}C^{16}O$ and $^{12}C^{18}O$ (Cambridge Isotopic Laboratories), and selected mixtures were used in different experiments. FTIR spectra were recorded at 0.5 cm^{-1} resolution on a Nicolet 750 spectrometer with 0.1 cm^{-1} accuracy using a HgCdTe detector. Matrix samples were annealed stepwise from 6 to 11 K, and selected samples were subjected to broadband photolysis by a medium-pressure mercury arc (Philips, 175 W, globe removed, 240−580 nm) and glass filters.

Results

Infrared spectra and density functional calculations of Co, Rh, and Ir reaction products with CO in excess neon will be presented. Sample deposition reveals strong CO absorption at 2140.8 cm^{-1} and weak CO^+, $(CO)_2^+$, and $(CO)_2^-$ absorptions at 2194.3, 2056.3, and 1517.4 cm^{-1} (not shown).[25,26]

Cobalt. Experiments were done with Co and 0.1% ^{12}CO and ^{13}CO in neon to complement earlier argon matrix experiments;[13] product absorptions are listed in Table 1, and a representative spectrum is shown in Figure 1.

10.1021/jp991400f CCC: $18.00
Published on Web 09/15/1999

TABLE 1: Infrared Absorptions (cm^{-1}) from Co-deposition of Laser-Ablated Co Atoms with CO Molecules in Excess Neon at 4 K

$^{12}C^{16}O$	$^{13}C^{16}O$	$R(^{12}C/^{13}C)$	assignment
2168.9	2121.0[a]	1.0226	$Co(CO)_2^+$
2165.5	2116.5	1.0232	$CoCO^+$
2067.2	2021.3	1.0227	$Co_x(CO)_y$
2059.9	2013.1	1.0232	$Co_2(CO)_8$
2052.4	2005.6	1.0233	$Co_2(CO)_8$
2047.1	2000.8	1.0231	$Co_2(CO)_8$
2029.6	1983.9	1.0230	$Co(CO)_4$
2022.2	1976.9	1.0229	$Co(CO)_4$
2019.0	1973.6	1.0230	$Co(CO)_4$ site
1991.5	1947.0	1.0229	$Co(CO)_3$
1973.9	1926.6	1.0246	CoCO
1962.2	1916.3	1.0240	$Co_x(CO)_y$
1947.7	1905.5	1.0221	$Co(CO)_2$ site
1945.6	1903.4	1.0222	$Co(CO)_2$
1920.9	1878.3	1.0227	$Co_x(CO)_y$
1899.8	1856.7	1.0232	$Co_x(CO)_y$
1894.8	1850.8	1.0238	$Co(CO)_4^-$
1847.1	1802.8	1.0246	$Co(CO)_2^-$
1831.5	1788.9	1.0238	$Co(CO)_3^-$ site
1829.1	1786.6	1.0238	$Co(CO)_3^-$
1820.2	1777.0	1.0243	$CoCO^-$
1789.2	1746.8	1.0243	$Co(CO)_2^-$
1787.0	1744.7	1.0242	$Co(CO)_2^-$ site

[a] 2134.0 cm^{-1} band for $Co(^{12}CO)(^{13}CO)^+$.

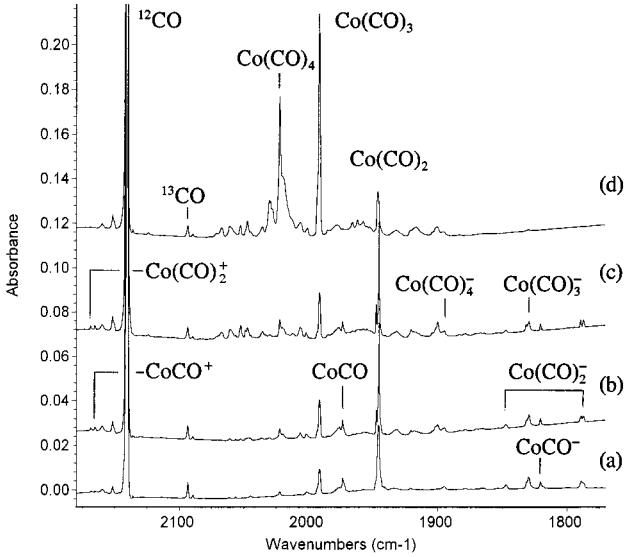

Figure 1. Infrared spectrum in the 2175−1775 cm^{-1} region for laser-ablated Co co-deposited with 0.1% CO in neon at 4 K after (a) sample co-deposited for 60 min, (b) annealing to 6 K, (c) annealing to 8 K, and (d) full-arc photolysis.

Rhodium. Laser-ablated Rh reactions with 0.1% and 0.2% CO (^{13}CO and $C^{18}O$) and a $^{12}CO + {}^{13}CO$ mixture were investigated. Product bands are listed in Table 2, and the cation, neutral, and anion products are illustrated in three spectral regions in Figures 2−4. The effect of doping with CCl_4 as a diagnostic for the identification of charged species[23,24] is shown for the cation region in Figure 2. Mixed isotopic spectra are presented for the neutral and anion product regions in Figures 5 and 6.

Three experiments were done with 0.5% CO in argon on a 7−8 K substrate, and spectra near 2000 cm^{-1} were a slightly better resolved version of the thermal atom spectra.[12] Argon matrix counterparts are given as footnotes in Table 2. No products were observed in the 2100 cm^{-1} region, but a family of bands appeared in the 1800 cm^{-1} region, which exhibited annealing and photolysis behavior like those in Figure 4. The latter bands did not appear with 0.05% CCl_4 present, but the 1901.5 cm^{-1} band grew in weakly on annealing. The shifts with ^{13}CO gave almost identical $^{12}C/^{13}C$ ratios to the neon matrix bands except the 1799.4 cm^{-1} band (1.0231 ratio).

Iridium. Similar investigations with laser-ablated Ir were done, the product absorptions are listed in Table 3, and infrared spectra for 0.1% CO are shown in Figures 7 and 8 and for the $^{12}CO + {}^{13}CO$ mixture in Figure 9.

Calculations. Density functional theory (DFT) calculations were done using the Gaussian 94 program[27] to contrast our earlier calculations on cobalt carbonyls[13] and other calculations on rhodium and iridium carbonys[17−21] and to support experimental band identifications. The BP86 and B3LYP functionals,[28,29] the D95* and 6-31+G* basis sets for C and O atoms, and the Los Alamos effective core potential (ECP) plus DZ basis set included in Gaussian 94 for Rh (28 electron core) and Ir (60 electron core) were employed.[32] Calculations were first performed on the monocarbonyl neutrals, cations, and anions, and the fully optimized results are listed in Tables 4 and 5 including frequencies from analytic second derivatives, isotopic frequencies, and ratios for comparison with experimental results. Previous calculations find $^2\Delta$ to be the ground state for all three MCO species,[17,21] and BP86 finds $^2\Sigma^+$ to be slightly lower for RhCO, but this energy difference is small. The harmonic carbonyl frequency for $^2\Delta$ RhCO calculated here with BP86 (2004.7 cm^{-1}) is lower than the B3LYP value (2085 cm^{-1})[17] and the CASMCSCF frequency (2107 cm^{-1});[21] this frequency agreement designates $^2\Delta$ as the ground state. However, our BP86 calculation predicts $^2\Delta$ IrCO at 2022.0 cm^{-1}, *higher* than RhCO, but the CASMCSCF calculation finds IrCO to be *lower* (2023 cm^{-1}).[21] The BP86 results fit experimental data better than the B3LYP and CASMCSCF calculations, as will be shown below. (These commonly used acronyms are defined in the references.)

In contrast, the $RhCO^-$ and $IrCO^-$ anions have the $^1\Sigma^+$ ground state instead of the $^3\Delta$ ground state found for $CoCO^-$ (Tables 4 and 5). All three MCO^+ cations converge to $^3\Delta$ and $M(CO)_2^+$ cations to $^3\Delta_g$ ground states, in agreement with ab initio results.[18] The BP86 functional finds four low states for the important $Rh(CO)_2$ species, but the B3LYP functional, which gives more accurate energies, suggests that $^2\Delta_g$ is the ground state (Table 6). Both $Rh(CO)_2^-$ and $Ir(CO)_2^-$ have the $^1A_1$ ground state calculated for $Co(CO)_2^-$. In contrast to trigonal $Co(CO)_3$, the Rh and Ir tricarbonyls and cations have T-shaped structures (C_{2v}), but their anions are all trigonal (D_{3h}) (Table 8). Recent DFT calculations by Ryeng et al.[33] find the most stable $Co(CO)_4$ structure to be of C_{3v} symmetry with the D_{2d} structure 3 kcal/mol higher, but our BP86 calculations for Rh and Ir indicate the reverse relationship (Table 9). The Rh and Ir tetracarbonyl anions are tetrahedral (T_d), whereas the cations are square planar (D_{4h}).

Finally, the $(OC)_2Rh(Cl)_2Rh(CO)_2$ molecule has been presented as a model for supported $Rh(CO)_2$ species,[3c,d] so the same BP86 calculation was performed on this molecule as a test case, and the results are summarized in Table 10. A similar calculation was done for the $Rh(CO)(Cl)(PH_3)_2$ complex, and the parameters are given in Table 11.

Discussion

The new metal carbonyl species will be identified from isotopic substitution and comparison to isotopic frequencies from density functional calculations. These experiments were done with low laser energy where the metal concentration is less than

TABLE 2: Infrared Absorptions (cm^{-1}) from Co-deposition of Laser-Ablated Rh Atoms with CO in Excess Neon at 4 K

$^{12}C^{16}O$	$^{13}C^{16}O$	$^{12}C^{18}O$	$^{12}C^{16}O + {}^{13}C^{16}O$	$R(^{12}C^{16}O/^{13}C^{16}O)$	$R(^{12}C^{16}O/^{12}C^{18}O)$	assignment
2194.3	2145.8			1.0226		CO^+
2184.7	2136.3	2133.1		1.0227	1.0242	$Rh(CO)_2^+$
2174.1	2125.0	2123.8		1.0231	1.0237	$RhCO^+$
2167.8	2119.9	2116.4		1.0226	1.0243	$Rh(CO)_3^+$
2163.1						$Rh(CO)_4^+$ site
2161.5	2114.4	2110.4		1.0222	1.0242	$Rh(CO)_4^+$
2160.1	2112.4	2108.9	2160.1,2112.4	1.0226	1.0243	$(CO)_x$
2151.9	2104.7	2100.7	2151.9, 2104.7	1.0224	1.0244	$(CO)_x$
2140.7	2093.6	2089.7	2140.7, 2093.6	1.0225	1.0244	CO
2040.6	1995.3	1992.3		1.0227	1.0242	?
2056.3	2010.9	2007.4	2056.3, 2018.4, 2010.9	1.0226	1.0244	$(CO)_2^+$
2033.2	1989.0	1984.4	2108.0, 2033.2, 2005.5, 1989.1	1.0222	1.0246	$Rh(CO)_2$ site
2031.0[a]	1986.8	1982.2	2105.0, 2031.0, 2003.2, 1986.8	1.0222	1.0246	$Rh(CO)_2$
2029.2	1983.2			1.0232		$Rh(CO)_3$
2023.5	1976.0	1979.6	2023.5, 1976.0	1.0240	1.0218	RhCO site
2022.5[b]	1975.1	1979.3	2022.5, 1974.9	1.0240	1.0218	RhCO
2021.5	1978.2	1973.5		1.0219	1.0243	$Rh(CO)_4$?
2020.3[c]	1976.0	1972.2	2020.4, 2010.3, 1995.3, 1989.1, 1976.0	1.0224	1.0244	$Rh(CO)_3$
2018.5	1974.3	1970.7		1.0224	1.0243	$Rh(CO)_4$
1950.6	1906.2	1906.1		1.0233	1.0233	$Rh_x(CO)_y$
1906.4[d]	1863.0	1863.6	1906.4, 1891.1, 1880.5, 1870.3, 1862.8	1.0233	1.0230	$Rh(CO)_4^-$
1902.7	1856.6			1.0248		$Rh(CO)_2^-$ site
1900.4	1854.7		1900.4, 1882.7, 1854.7	1.0246		$Rh(CO)_2^-$
1867.9	1825.5	1825.8		1.0232	1.0231	$Rh(CO)_3^-$
1864.8[e]	1822.4	1822.5	1864.8, 1845.3, 1833.0, 1822.4	1.0233	1.0232	$Rh(CO)_3^-$
1862.8	1820.6	1820.9	1862.8, 1843.5, 1830.8, 1820.5	1.0232	1.0231	$Rh(CO)_3^-$
1843.8	1804.0	1802.6		1.0221	1.0229	$Rh_x(CO)_y$
1828.6[f]	1782.7	1793.7	1828.4, 1782.7	1.0257	1.0195	$RhCO^-$
1826.7	1781.2	1791.9	1826.6, 1781.2	1.0255	1.0194	$RhCO^-$ site
1825.8	1783.4	1785.3		1.0238	1.0227	Rh_xCO
1816.7[g]	1774.8	1776.6	1816.6, 1790.2, 1774.8	1.0236	1.0226	$Rh(CO)_2^-$
1814.4	1772.6	1774.2	1814.5, 1788.2, 1772.7	1.0236	1.0227	$Rh(CO)_2^-$ site
1813.2	1771.3	1773.2	1813.2, 1786.8, 1771.3	1.0237	1.0226	$Rh(CO)_2^-$ site
1768.5	1728.2	1728.9		1.0233	1.0229	$Rh_x(CO)_y$ site
1766.5	1726.2	1725.8		1.0233	1.0236	$Rh_x(CO)_y$?
1517.4	1484.2	1481.2	1517.4, 1499.4, 1484.2	1.0224	1.0244	$(CO)_2^-$
1516.4	1483.0	1490.4	1516.3, 1498.1, 1483.0	1.0225	1.0243	$(CO)_2^-$ site

[a] Argon matrix ^{12}CO counterpart: 2014.6 cm^{-1}. [b] Argon matrix ^{12}CO counterpart: 2007.6 cm^{-1}. [c] Argon matrix ^{12}CO counterparts: 2011 and 2008.3 cm^{-1}. [d] Argon matrix ^{12}CO counterpart: 1901.5 cm^{-1}. [e] Argon matrix ^{12}CO counterpart: 851.9 cm^{-1}. [f] Argon matrix ^{12}CO counterpart: 1813.7 cm^{-1}. [g] Argon matrix ^{12}CO counterpart: 1799.4 cm^{-1}.

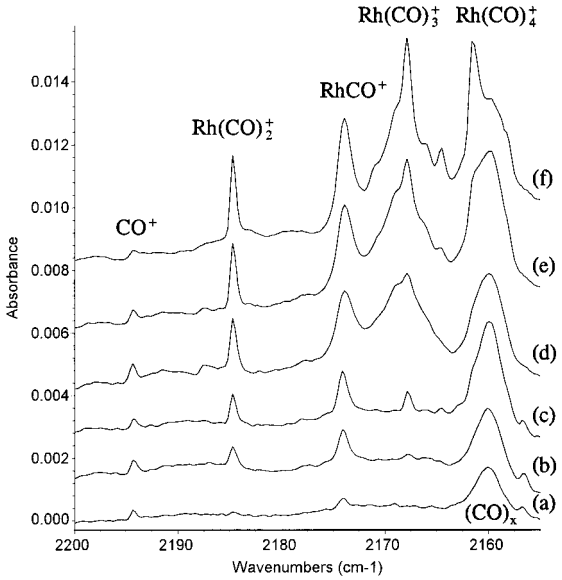

Figure 2. Infrared spectrum in the 2200−2155 cm^{-1} region for laser-ablated Rh co-deposited with CO in neon at 4 K after (a) 0.1% CO sample co-deposited for 60 min, (b) 0.2% CO sample deposited for 60 min, (c) annealing to 8 K, (d) 0.2% CO sample with 0.1% CCl_4 co-deposited for 60 min, (e) annealing to 8 K, and (f) annealing to 11 K.

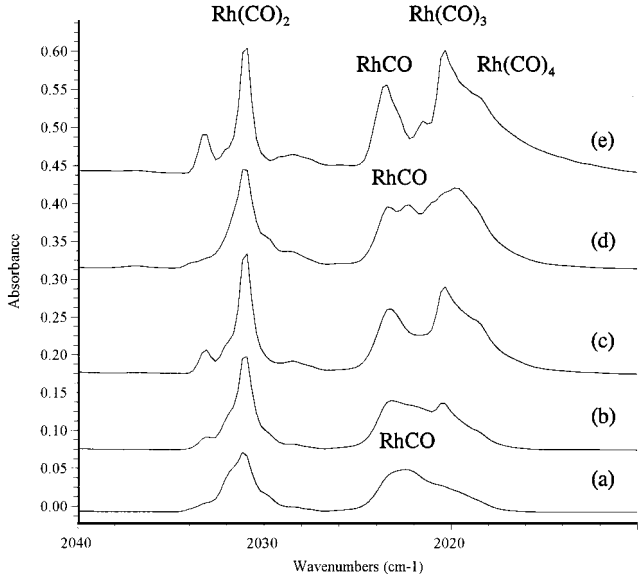

Figure 3. Infrared spectrum in the 2040−2010 cm^{-1} region for laser-ablated Rh co-deposited with CO in neon at 4 K after (a) 0.1% CO sample co-deposited for 60 min, (b) 0.2% CO sample deposited for 60 min, (c) annealing to 8 K, (d) 0.2% CO sample with 0.1% CCl_4 co-deposited for 60 min, and (e) annealing to 10 K.

the CO concentration, and the major deposition products are monometal carbonyl species as confirmed by DFT frequency calculations. However, on annealing, weaker features grow that are due to dimetal species. The spectrum for the cobalt system

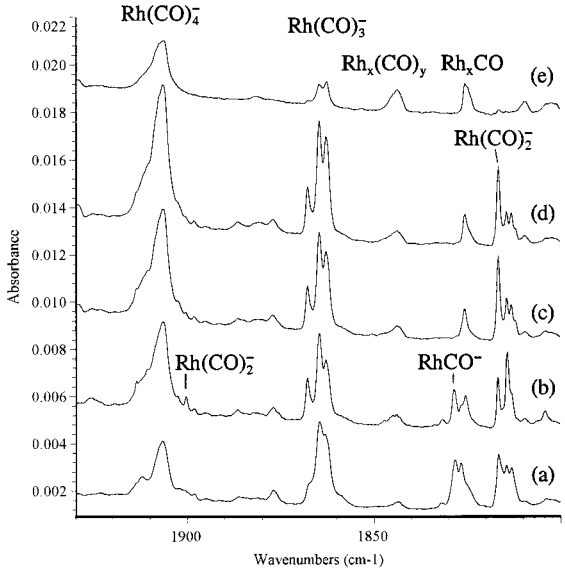

Figure 4. Infrared spectrum in the 1930−1800 cm^{-1} region for laser-ablated Rh co-deposited with CO in neon at 4 K after (a) 0.1% CO sample co-deposited for 60 min, (b) 0.2% CO sample deposited for 60 min, (c) $\lambda > 380$ nm photolysis, (d) $\lambda > 290$ nm photolysis, and (e) full-arc photolysis.

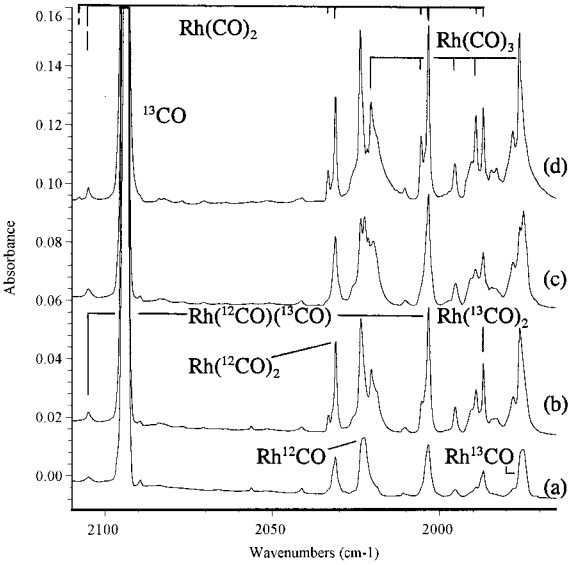

Figure 5. Infrared spectrum in the 2120−1965 cm^{-1} region for laser-ablated Rh co-deposited with 0.08% ^{12}CO and 0.08% ^{13}CO in neon at 4 K after (a) sample deposited for 45 min, (b) annealing to 8 K, (c) full-arc photolysis, and (d) annealing to 10 K.

(Figure 1) shows the minor contribution of $Co_2(CO)_8$ absorptions near 2050 cm^{-1} to the overall product spectrum. Annealing produces weak unidentified bands that are ascribed to $M_x(CO)_y$ species in all metal systems.

Cobalt. The four neutral $Co(CO)_x$ carbonyls were identified in previous thermal and laser ablation experiments.[11,13] The neon matrix counterparts (Figure 1) are *blue-shifted* 16.6, 24.8, 8.3, 5.6, and 6.1 cm^{-1}, respectively, for $x = 1-4$ (two modes for $Co(CO)_4$). These argon-to-neon blue shifts are comparable to those observed for the $Fe(CO)_x$ species and are larger for the smaller species, which are expected to interact more strongly with the matrix.[24,34] The slightly larger difference for $Co(CO)_2$ may indicate a change in the OC−Co−CO angle, since dipole moment and matrix interaction will change accordingly. The four carbonyl anion frequencies are observed in solid neon *blue-shifted* 16.2, 18.1, 2.2, and 4.8 cm^{-1}, respectively, from the

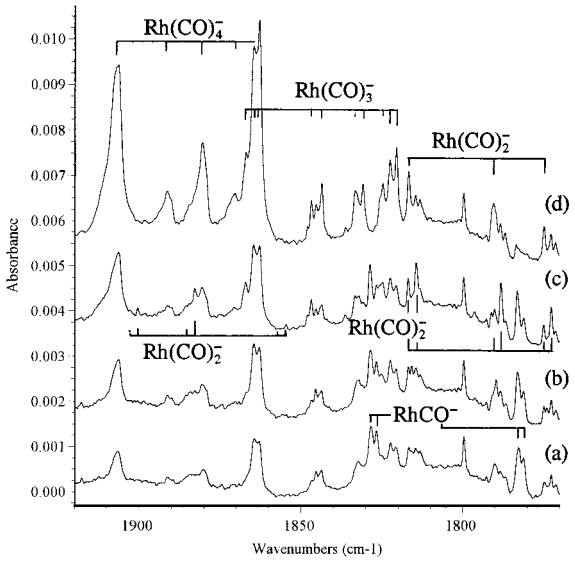

Figure 6. Infrared spectrum in the 1920−1770 cm^{-1} region for laser-ablated Rh co-deposited with 0.08% ^{12}CO and 0.08% ^{13}CO in neon at 4 K after (a) sample deposited for 45 min, (b) annealing to 6 K, (c) annealing to 8 K, and (d) $\lambda > 290$ nm photolysis.

argon matrix values, and again, comparable behavior was found for the iron carbonyl anions in solid argon and neon.[24,34]

Metal cations are more mobile in the less polarizable neon matrix during deposition, and as a consequence, metal cation carbonyl yields are higher in solid neon.[24,34] The two sharp bands at 2165.5 and 2168.9 cm^{-1} are due to $CoCO^+$ and $Co(CO)_2^+$ for the following reasons. Photolysis destroys these bands along with the anion bands in a photoneutralization process. Higher temperature annealing (10 K, not shown) favors the 2168.9 cm^{-1} band over the 2165.5 cm^{-1} absorption. In the ^{13}CO experiment with 10% ^{12}CO, the 2165.5 cm^{-1} band is a factor of 5 stronger than the 2168.9 cm^{-1} band, and a 2134.0 cm^{-1} mixed isotopic band is observed for $Co(^{12}CO)(^{13}CO)^+$ along with $Co(^{13}CO)_2^+$ at 2121.0 cm^{-1} (Table 1). Our BP86 calculations predict $^3\Delta_g$ $Co(^{12}CO)_2^+$ to absorb at 2136.4 cm^{-1}, the mixed isotope at 2102.4 cm^{-1}, and $Co(^{13}CO)_2^+$ at 2088.3 cm^{-1}. Scaling these isotopic bands by 1.0152 fits the observed frequencies. Our BP86 calculation predicts $CoCO^+$ at 2147.0 cm^{-1} with a ^{12}C/^{13}C isotopic frequency ratio of 1.0237, which is just under the observed 2165.5 cm^{-1} value (scale factor 1.0086). The observed ^{12}C/^{13}C isotopic frequency ratio (1.0232) is in near agreement, and the calculated ^{12}C/^{13}C ratio predicts a 50.1 cm^{-1} ^{13}CO shift, whereas a 49.0 cm^{-1} shift is observed. Our BP86 calculations support the assignments to $CoCO^+$ and $Co(CO)_2^+$ and confirm that the metal carbonyl cations absorb about 200 cm^{-1} above the neutral carbonyls, which are about 160 cm^{-1} higher than the carbonyl anions. A similar relationship has been found for iron carbonyls[24,34−36] and for rhodium[17] and iridium carbonyls.

Rhodium. The two bands at 2031.0 and 2022.5 cm^{-1} with Rh and CO in neon increase on annealing and acquire site splittings at 2033.2 and 2023.5 cm^{-1} (Figure 3). The strongest new band is produced on annealing at 2020.3 cm^{-1} with a 2018.5 cm^{-1} shoulder. The mixed ^{12}CO + ^{13}CO isotopic spectra (Figure 5) show a doublet at 2022.5 and 1975.1 cm^{-1} for a single carbonyl and a sharp 2031.0, 2003.2, 1986.8 cm^{-1} triplet for a two-equivalent-carbonyl vibration. These bands are assigned to RhCO and the antisymmetric C−O stretching mode of $Rh(CO)_2$. The weak symmetric C−O stretching mode of $Rh(^{12}CO)(^{13}CO)$ is observed at 2105.0 cm^{-1} with the identical matrix site structure as the antisymmetric rhodium dicarbonyl

TABLE 3: Infrared Absorptions (cm^{-1}) from Co-deposition of Laser-Ablated Ir Atoms and CO in Excess Neon at 4 K

$^{12}C^{16}O$	$^{13}C^{16}O$	$^{12}C^{18}O$	$^{12}C^{16}O + {}^{13}C^{16}O$	$R(^{12}C^{16}O/^{13}C^{16}O)$	$R(^{12}C^{16}O/^{12}C^{18}O)$	assignment
2156.5	2109.0	2105.5		1.0225	1.0242	$IrCO^+$
2153.8	2106.1	2102.9		1.0226	1.0242	$Ir(CO)_2^+$
2024.5	1974.4	1984.9	2024.5, 1974.4	1.0254	1.0200	IrCO
2023.2	1973.1	1983.7	2023.2, 1973.1	1.0254	1.0199	IrCO site
2021.3	1972.7	1977.3	2020.4, 1973.0	1.0246	1.0223	$Ir(CO)_3$
2017.0	1972.7	1968.9	2016.9, 1989.9, 1972.7	1.0225	1.0244	$Ir(CO)_2$ site
2015.9	1971.6	1967.8		1.0225	1.0244	$Ir(CO)_2$ site
2014.5	1970.2	1966.5	2109.4, 2014.5, 1987.5, 1970.2	1.0225	1.0244	$Ir(CO)_2$
2012.0	1967.3	1964.9	2012.0, 1982.3, 1967.3	1.0227	1.0240	$Ir(CO)_3$
2010.5	1965.2	1964.9	2010.5, 1998.5, 1981.4, 1965.2	1.0231	1.0232	$Ir(CO)_4$
1901.8	1857.3	1860.4	1901.9, 1885.7, 1874.4, 1862.7, 1857.8	1.0240	1.0223	$Ir(CO)_4^-$
1895.3	1854.7	1848.9	1895.3, 1871.5, 1854.7	1.0219	1.0251	$Ir_2(CO)_2$-t
1881.5	1837.5	1840.6	1881.5, 1837.7	1.0239	1.0222	Ir_xCO
1878.5	1834.7	1837.6	1878.4, 1834.8	1.0239	1.0223	Ir_xCO site
1868.3	1827.8	1823.1		1.0222	1.0248	$Ir_x(CO)_y$
1863.7	1820.5			1.0237		$Ir(CO)_3^-$ site
1860.4	1817.1	1819.5	1860.1, 1842.1, 1828.2, 1817.4	1.0238	1.0225	$Ir(CO)_3^-$
1847.1	1805.6	1804.6	1847.0, 1822.1, 1805.6	1.0230	1.0236	$Ir_x(CO)_2$
1842.6	1794.3	1809.0	1842.6, 1794.3	1.0269	1.0186	$IrCO^-$
1818.1	1775.0	1779.2	1818.1, 1790.9, 1775.1	1.0243	1.0219	$Ir(CO)_2^-$
1815.4	1772.6	1776.9	1815.4, 1788.8, 1772.7	1.0241	1.0217	$Ir(CO)_2^-$ site
1797.9	1758.7	1755.3	1797.9, 1775.4, 1758.7	1.0223	1.0243	$Ir_2(CO)_2$-b

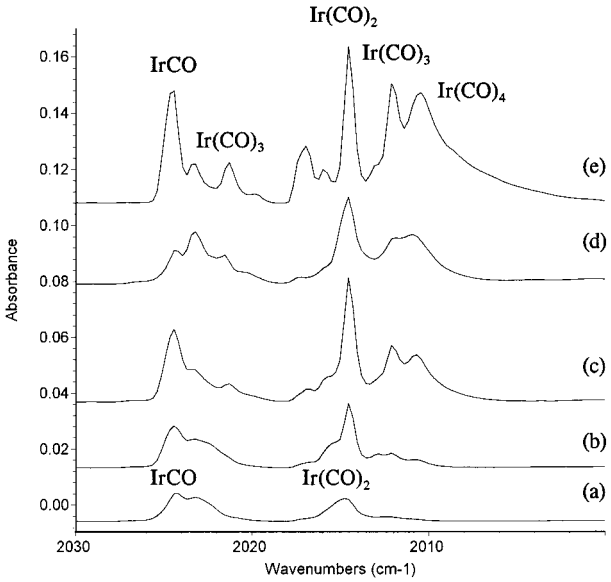

Figure 7. Infrared spectrum in the 2030−2000 cm^{-1} region for laser-ablated Ir co-deposited with 0.1% CO in neon at 4 K after (a) sample deposited for 60 min, (b) annealing to 6 K, (c) annealing to 8 K, (d) full-arc photolysis, and (e) annealing to 11 K.

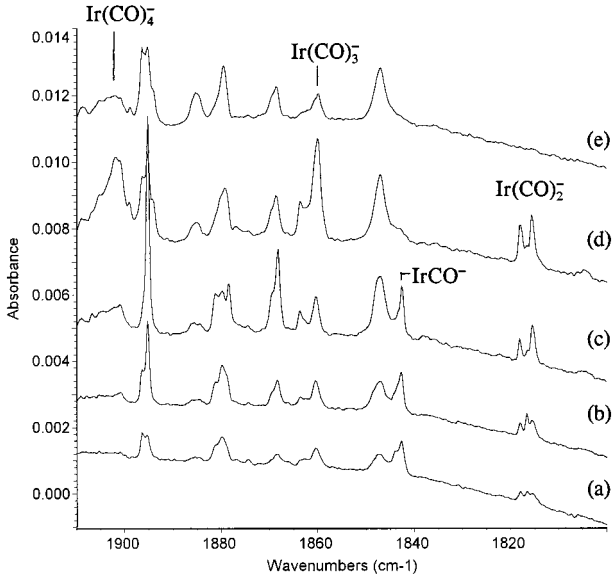

Figure 8. Infrared spectrum in the 1919−1800 cm^{-1} region for laser-ablated Ir co-deposited with 0.1% CO in neon at 4 K after (a) sample deposited for 60 min, (b) annealing to 6 K, (c) annealing to 8 K, (d) $\lambda > 290$ nm photolysis, and (e) full-arc photolysis.

isotopic bands (connected to the stronger antisymmetric modes by the top bar in Figure 5).

These assignments are confirmed by DFT calculations. Although the $^2\Sigma^+$ state is calculated to be slightly lower than $^2\Delta$ at the BP86 level, earlier calculations found the $^2\Delta$ state to be lower.[17,21] The frequency match is much better for the $^2\Delta$ state but the isotopic $^{12}C/^{13}C$ and $^{16}C/^{18}C$ frequency ratios are the same for both states, which are very close to the observed ratios for RhCO. Our BP86 calculations predict four low-energy $Rh(CO)_2$ states, but the $^2\Delta_g$ state antisymmetric C−O stretching mode calculated at 2004.1 cm^{-1} (Table 7A) fits the 2031.0 cm^{-1} observed value better, and B3LYP calculations, which give more accurate energies, predict the $^2\Delta_g$ ground state. Furthermore, the symmetric C−O stretching mode for $Rh(^{12}CO)(^{13}CO)$ is calculated to have 8% of the intensity of the antisymmetric C−O stretching mode and the observed 2105.0 cm^{-1} band is 7% as intense as the 2003.2 cm^{-1} band! Scale factors for the three isotopic antisymmetric modes, 1.0134, 1.0143, 1.0143, and for the symmetric mode, 1.0177, are appropriate for this level of theory.[37] The observation of a symmetric C−O mode for $Rh(^{12}CO)(^{13}CO)$ and not for $Rh(^{12}CO)_2$ or $Rh(^{13}CO)_2$ strongly indicates a linear structure for the isolated $Rh(CO)_2$ molecule, which is suggested by DFT to be the $^2\Delta_g$ state.

The strong band at 2020.3 cm^{-1} after annealing (Figure 3) is assigned to $Rh(CO)_3$. Our BP86 calculations predict a T-shaped (C_{2v}) structure with the strongest (b_2) absorption at 1981.4 cm^{-1}. Of more importance, the calculations for the four mixed ^{12}CO, ^{13}CO isotopic molecules predict two strong bands unshifted from pure isotopic values plus two weaker intermediate bands about 30 and 34 cm^{-1} below the $Rh(^{12}CO)_3$ absorption, and the marked bands at 1995.3 and 1989.1 cm^{-1} in Figure 5 are in very good agreement. The weaker 2010.3 cm^{-1} band is due to a symmetric mode of $Rh(^{12}CO)(^{13}CO)_2$. A weaker 2029.2 cm^{-1} band is tentatively assigned to the a_1 mode of $Rh(CO)_3$.

The 2018.5 cm^{-1} shoulder that increases on annealing is appropriate for $Rh(CO)_4$ in solid neon on the basis of previous thermal Rh atom work, which conclusively identified $Rh(CO)_4$ at 2010 cm^{-1} in solid argon with 10% CO and at 2012 cm^{-1} in

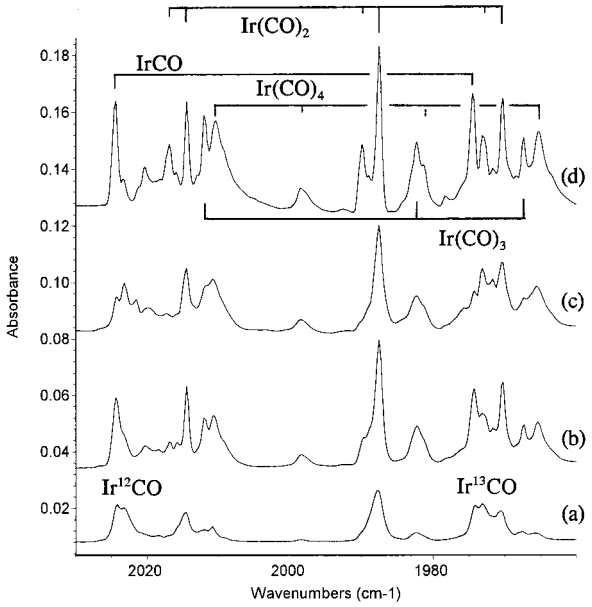

Figure 9. Infrared spectrum in the 2030−1960 cm^{-1} region for laser-ablated Ir co-deposited with 0.08% ^{12}CO and 0.08% ^{13}CO in neon at 4 K after (a) sample deposited for 45 min, (b) annealing to 8 K, (c) full-arc photolysis, and (d) annealing to 10 K.

TABLE 4: Relative Energies, Bond Lengths, and Mulliken Charges Calculated (BP86) for the MCO, MCO^+, and MCO^- (M = Co, Rh, Ir) Monocarbonyls[a]

molecule	state	energy (kcal/mol)	bond length[b] (Å)	Mulliken charge on atom M	C	O
CoCO	$^2\Delta$ ($\sigma^2\delta^3\pi^4$)	0	1.682, 1.170	−0.09	0.25	−0.16
$CoCO^-$	$^3\Delta$ ($\sigma^1\delta^4\pi^4$)	−22.3	1.712, 1.191	−0.67	−0.10	−0.23
$CoCO^+$	$^3\Delta$ ($\sigma^1\delta^3\pi^4$)	+179.7	1.822, 1.139	0.68	0.24	0.08
RhCO	$^2\Delta$ ($\sigma^2\delta^3\pi^4$)	0	1.822, 1.177	0.12	−0.02	−0.10
RhCO	$^2\Sigma^+$ ($\sigma^1\delta^4\pi^4$)	−0.8	1.789, 1.184	0.09	0.04	−0.13
$RhCO^-$	$^1\Sigma^+$ ($\sigma^2\delta^4\pi^4$)	−34.5	1.736, 1.212	−0.90	0.17	−0.27
$RhCO^+$	$^3\Delta$ ($\sigma^1\delta^3\pi^4$)	+193.3	1.903, 1.152	0.88	0.05	0.07
IrCO	$^2\Delta$ ($\sigma^2\delta^3\pi^4$)	0	1.768, 1.183	0.25	−0.14	−0.11
$IrCO^-$	$^1\Sigma^+$ ($\sigma^2\delta^4\pi^4$)	−35.5	1.730, 1.219	−0.79	0.09	−0.30
$IrCO^+$	$^3\Delta$ ($\sigma^1\delta^3\pi^4$)	+210.3	1.823, 1.159	1.06	−0.12	0.06
RhCO	$^2\Delta$	0	1.824, 1.173	0.25	−0.07	−0.18
RhCO	$^2\Sigma^+$	−0.7	1.791, 1.180	0.17	0.04	−0.21
$RhCO^-$	$^1\Sigma^+$	−37.2	1.736, 1.209	−0.96	0.17	−0.20
$RhCO^+$	$^3\Delta$	+193.9	1.913, 1.147	0.94	0.13	−0.07
IrCO	$^2\Delta$	0	1.769, 1.179	0.10	0.16	−0.26
$IrCO^-$	$^1\Sigma^+$	−38.8	1.729, 1.215	−0.07	−0.60	−0.33
$IrCO^+$	$^3\Delta$	+210.5	1.831, 1.154	0.90	0.25	−0.15

[a] Co calculations used 6-311+G* basis for C and O, first group of Rh and Ir calculations used D95* basis for C and O, and second (bottom) group for Rh and Ir used 6-31+G*. [b] Linear molecules, first is M−C and second is C−O bond length.

pure solid CO.[12] Our BP86 calculations suggest that $Rh(CO)_4$ has the D_{2d} structure, but the C_{3v} structure is slightly higher in energy (Table 9). The D_{2d} structure has a very strong (e) mode calculated at 1988.0 cm^{-1}, which is 1.5% low and in line with the other $Rh(CO)_x$ frequencies calculated here.

Unfortunately, $Rh(CO)_3$ is not correctly identified by the earlier workers owing to band congestion and the failure to resolve mixed isotopic counterparts. However, with 0.2% CO in argon, the sharp dominant band at 2008.0 cm^{-1} assigned to RhCO is in good agreement with our 2007.6 cm^{-1} argon and 2022.5 cm^{-1} neon matrix values. It is important to note that the thermal rhodium atom work failed to produce the bands we assign next to the $Rh(CO)_x^-$ anions.

The 1816.7, 1828.6, 1864.8, and 1906.4 cm^{-1} bands in Figure 4 are due to carbonyl vibrations of the $Rh(CO)_x^-$ anions. These bands *decreased* to less than 10% of their absorbance when the sample was doped with 0.01% of the electron-trapping molecule CCl_4 and are 17.1, 14.9, 12.9, and 4.9 cm^{-1} higher than argon matrix counterparts in laser ablation studies. First, the 1828.6 cm^{-1} band decreases slightly on annealing to 8 K, while the others increase, and disappears on $\lambda > 380$ nm photolysis while the others slightly increase. The 1828.6 cm^{-1} band and 1826.7 cm^{-1} satellite give a doublet mixed isotopic absorption (Figure 6, bars connect isotopic counterparts) for the vibration of a single carbonyl. Our BP86 calculations predict the $RhCO^-$ absorption at 1843.6 cm^{-1} with unique large 1.0268 and small 1.0186 isotopic $^{12}C/^{13}C$ and $^{16}O/^{18}O$ frequency ratios, which are in excellent agreement with the observed 1.0257 and 1.0195 ratios. This large $^{12}C/^{13}C$ and small $^{16}O/^{18}O$ isotopic ratio for a C−O stretching mode is due to the antisymmetric nature of C vibrating between Rh and O, the Rh−C bond strength, and the coupling of Rh−C and C−O vibrations.

A 1814.4 cm^{-1} site of the 1816.7 cm^{-1} band and an associated 1900.4 cm^{-1} feature increase on 8 K annealing, and the 1816.7 cm^{-1} band decreases 5% on $\lambda > 290$ nm photolysis while the remaining two bands slightly increase. The mixed ^{12}CO, ^{13}CO spectrum reveals triplet patterns and two equivalent carbonyls for these absorptions and suggests the $Rh(CO)_2^-$ assignment. Our BP86 calculation predicts 1813.2 cm^{-1} (b_2) and 1879.6 cm^{-1} (a_1) modes with 4.5/1 relative intensity and isotopic frequency ratios that are in excellent agreement with the observed spectrum.

The structured 1864.8 cm^{-1} band is 80% destroyed on full-arc photolysis. The isotopic shifts denote a carbonyl motion, and the four-band mixed isotopic pattern is characteristic of the doubly degenerate (e) vibration of a trigonal species, which is predicted at 1848.3 cm^{-1} at the BP86 level. Accordingly, the 1864.8 cm^{-1} band is assigned to $Rh(CO)_3^-$.

The 1906.4 cm^{-1} feature is 65% destroyed by full-arc photolysis. The five-band mixed isotopic spectrum is characteristic of the triply degenerate (t_2) vibration of a tetrahedral species,[38] which is calculated for tetrahedral $Rh(CO)_4^-$ at 1882.7 cm^{-1} using the BP86 functional. This assignment is in agreement with the observation of $Rh(CO)_4^-$ in THF solution[15] at 1900 cm^{-1}. The $Rh(CO)_x^-$ anion absorptions are fit by our BP86 calculations with scale factors ranging from 0.992 to 1.013.

The 2161.5, 2167.8, 2174.1, and 2184.7 cm^{-1} bands are assigned to the $Rh(CO)_x^+$ cations. These bands along with CO^+ (2194.3 cm^{-1})[25] were enhanced on doping with CCl_4 to capture electrons that might neutralize cations;[24,34] curves b and d of Figure 2 are spectra of deposited 0.2% CO samples. Annealing to 8 K with CCl_4 present *markedly* increased the 2167.8 cm^{-1} band, and a further annealing to 11 K *markedly* increased the 2161.5 cm^{-1} shoulder absorption. Another experiment with 0.1% CO (Figure 2a) showed the 2174.1 cm^{-1} band to be the strongest product in this region, but stepwise annealing to 6 and 8 K (not shown) increased the 2184.7 cm^{-1} band more than the 2174.1 cm^{-1} absorption and produced a weak 2167.8 cm^{-1} band. These bands all show carbonyl isotopic ratios, but band congestion precludes observation of mixed isotopic counterparts, so the order of band evolution with increasing CO concentration and on annealing provides the experimental evidence for x values. The 2174.1 cm^{-1} band is assigned to $RuCO^+$, the 2184.7 cm^{-1} absorption to $Ru(CO)_2^+$, the 2167.8 cm^{-1} band to $Ru(CO)_3^+$, and the 2161.5 cm^{-1} feature to $Ru(CO)_4^+$. These assignments are all strongly supported by the BP86 frequency calculations reported here. Scale factors (observed/calculated) range from

TABLE 5: Isotopic Frequencies (cm^{-1}), Intensities (km/mol), and Isotopic Frequency Ratios Calculated for the Monocarbonyl Structures Described in Table 4[a]

molecule	frequency (intensity) $^{12}C^{16}O$	$^{13}C^{16}O$	$^{12}C^{18}O$	$R(^{12}C/^{13}C)$	$R(^{16}O/^{18}O)$
CoCO ($^2\Delta$)	1980.5 (697) (σ)	1931.8 (660)	1939.8 (674)	1.0252	1.0210
	598.9 (4) (σ)	593.3 (4)	583.1 (3)	1.0094	1.0271
	358.0 (11) (π)	347.2 (10)	353.9 (11)	1.0311	1.0116
$CoCO^-$ ($^3\Delta$)	1836.2 (912) (σ)	1791.0 (876)	1798.5 (863)	1.0252	1.0210
	552.1 (4) (σ)	546.9 (4)	537.5 (4)	1.0095	1.0272
	200.0 (67) (π)	194.0 (64)	197.6 (66)	1.0309	1.0121
$CoCO^+$ ($^3\Delta$)	2147.0 (233) (σ)	2097.2 (218)	2098.1 (228)	1.0237	1.0233
	452.5 (4) (σ)	447.6 (3)	441.5 (3)	1.0109	1.0249
	314.2 (1) (π)	304.9 (1)	310.3 (1)	1.0305	1.0126
RhCO ($^2\Delta$)	2004.7 (504) (σ)	1955.8 (478)	1962.6 (487)	1.0250	1.0215
	534.5 (2) (σ)	528.3 (2)	518.6 (2)	1.0117	1.0307
	309.0 (12) (π)	299.7 (11)	305.4 (12)	1.0310	1.0118
RhCO ($^2\Sigma^+$)	1962.8 (486) (σ)	1914.8 (461)	1921.9 (469)	1.0251	1.0213
	555.9 (1) (σ)	549.5 (1)	539.3 (1)	1.0116	1.0308
	344.2 (7) (π)	333.7 (6)	340.1 (7)	1.0315	1.0121
$RhCO^-$ ($^1\Sigma^+$)	1843.6 (757) (σ)	1795.5 (725)	1810.0 (719)	1.0268	1.0186
	624.9 (6) (σ)	618.8 (5)	604.6 (6)	1.0099	1.0336
	368.6 (19) (π)	357.3 (17)	364.4 (19)	1.0316	1.0115
$RhCO^+$ ($^3\Delta$)	2129.4 (238) (σ)	2079.9 (223)	2081.1 (234)	1.0238	1.0232
	437.0 (7) (σ)	431.5 (7)	424.7 (6)	1.0127	1.0290
	314.2 (0.4) (π)	304.8 (0.4)	310.4 (0.4)	1.0308	1.0122
IrCO ($^2\Delta$)	2022.0 (548) (σ)	1969.7 (517)	1984.2 (532)	1.0266	1.0191
	638.8 (3) (σ)	631.4 (3)	616.4 (2)	1.0117	1.0363
	426.4 (2) (σ)	413.4 (2)	421.3 (3)	1.0314	1.0121
$IrCO^-$ ($^1\Sigma^+$)	1866.4 (868) (σ)	1815.1 (824)	1836.2 (836)	1.0283	1.0164
	675.6 (0.2) (σ)	668.9 (0.1)	650.3 (0.4)	1.0100	1.0389
	440.4 (1) (π)	426.9 (1)	435.3 (2)	1.0316	1.0117
$IrCO^+$ ($^3\Delta$)	2128.2 (326) (σ)	2075.9 (304)	2084.2 (322)	1.0252	1.0211
	573.5 (15) (σ)	566.1 (15)	554.5 (13)	1.0131	1.0343
	396.7 (0.1) (π)	384.7 (0.1)	391.9 (0.1)	1.0312	1.0122
RhCO ($^2\Delta$)	1999.6 (522)	1951.2 (494)	1957.2 (503)	1.0248	1.0217
RhCO ($^2\Sigma$)	1956.2 (504)	1908.8 (478)	1914.9 (486)	1.0248	1.0216
$RhCO^-$ ($^1\Sigma^+$)	1823.2 (892)	1775.9 (855)	1789.4 (847)	1.0266	1.0189
$RhCO^+$ ($^3\Delta$)	2135.7 (230)	2086.4 (215)	2086.8 (225)	1.0236	1.0234
IrCO ($^2\Delta$)	2011.3 (559)	1959.8 (527)	1973.0 (543)	1.0263	1.0194
$IrCO^-$ ($^1\Sigma^+$)	1843.2 (1008)	1793.0 (957)	1812.5 (972)	1.2280	1.0169
$IrCO^+$ ($^3\Delta$)	2124.8 (313)	2073.1 (292)	2080.0 (309)	1.0249	1.0215

[a] First calculations for Rh and Ir used the D95* basis set for oxygen and carbon, and the last seven lines give carbonyl frequencies using the 6-31+G* basis set.

1.021 to 1.032, which is appropriate for this density functional and basis set.[37]

Iridium. The strongest two bands on deposition with Ir and 0.1% CO in neon at 2024.5 and 2014.5 cm^{-1} increase on annealing and acquire satellites at 2023.2 and 2017.0 cm^{-1}, and new bands also appear at 2021.3, 2012.0, and 2010.5 cm^{-1} (Figure 7). The mixed isotopic spectrum shows a doublet for the 2024.5 cm^{-1} band and a triplet for the 2014.5 cm^{-1} absorption, which identifies IrCO and $Ir(CO)_2$, respectively (Figure 9, bars connect isotopic counterparts). As for rhodium, the symmetric C−O stretching mode for the mixed isotopic dicarbonyl was also detected (2109.4 cm^{-1}, not shown). These assignments are confirmed by BP86 calculations, which predict strong absorptions at 2022.0 and 1998.0 cm^{-1}, respectively, with isotopic frequency ratios in very good agreement between calculated and observed, which are slightly different for the metal monocarbonyl and dicarbonyl molecules (Tables 2, 3, 5, and 7).

In another experiment with 0.5% CO, the strongest band on deposition is 2010.5 cm^{-1} with a 2012.0 cm^{-1} shoulder; these two bands are resolved on annealing and the 2010.5 cm^{-1} absorption dominates the spectrum (not shown). The 2012.0 and 2010.5 cm^{-1} absorptions are assigned to $Ir(CO)_3$ and $Ir(CO)_4$, respectively. The 2012.0 cm^{-1} band shows a mixed isotopic band at 1982.3 cm^{-1} (Figure 9), and the weaker 2021.3 cm^{-1} band follows the 2012.0 cm^{-1} band on annealing and CO concentration changes (Figure 7). Our BP86 calculations predict 1980.6 cm^{-1} (b_2) and 2005.5 cm^{-1} (a_1) modes with 2/1 relative intensities for $Ir(CO)_3$, in a C_{2v} structure, which are in very good agreement with experimental results. The 2010.5 cm^{-1} band, which dominates on final annealing (Figure 7), is the neon matrix counterpart for the $Ir(CO)_4$ band observed in solid argon at 2002.6 cm^{-1} with thermal iridium atoms.[12] Unfortunately, insufficient resolution of bands assigned earlier[12] to $Ir(CO)_{1-3}$ in solid argon and the lack of mixed isotopic data raise doubts about their assignments. The 1998.5 cm^{-1} mixed isotopic feature and possibly the shoulder absorption at 1981 cm^{-1} are due to $Ir(^{12,13}CO)_4$, and this pattern is appropriate for the doubly degenerate mode of a C_{3v} molecule.[38] Finally, there appears to be additional absorption at 2017 cm^{-1} in solid neon that may be associated with the 2010.5 cm^{-1} $Ir(CO)_4$ band.

The anion region is complicated by the presence of polynuclear clusters with bridged carbonyls, but the iridium carbonyl anion absorptions can be identified from their destruction on $\lambda > 290$ nm or full-arc photolysis and their reduction to less than 10% on CCl_4 doping, which has little effect on neutral clusters (Figure 8). The 1842.6, 1815.4, 1860.4, and 1901.8 cm^{-1} bands are assigned to the $Ir(CO)_x^-$ anions, $x = 1, 2, 3, 4$, respectively. Note that $IrCO^-$ is destroyed by $\lambda > 290$ nm photolysis, which slightly increases $Ir(CO)_2^-$ and increases $Ir(CO)_{3,4}^-$ by a factor of 2. This photolysis behavior is consistent with an increase in photon energy for photodetachment with increasing x value

TABLE 6: Calculated Relative Energies (kcal/mol) and Geometries

(A) For $M(CO)_2$, $M(CO)_2^-$, and $M(CO)_2^+$ Using the BP86 Functional[a]

molecule	state	energies	geometries (M−C, C−O, ∠C−M-C, ∠M−C−O)
$Co(CO)_2^+$	$^3\Delta_g$	+182.5	1.897 Å, 1.135 Å, 180°, 180°
$Rh(CO)_2$	$^2B_2$	0.0	1.860 Å, 1.176 Å, 100.3°, 168.5°
$Rh(CO)_2$	$^2A_1$	+2.4	1.913 Å, 1.172 Å, 145.1°, 167.8°
$Rh(CO)_2$	$^2\Sigma_g^+$	+4.2	1.931 Å, 1.167 Å, 180°, 180°
$Rh(CO)_2$	$^2\Delta_g$	+5.6	1.946 Å, 1.164 Å, 180°, 180°
$Rh(CO)_2^-$	$^1A_1$	−55.7	1.851 Å, 1.201 Å, 126.3°, 161.4°
$Rh(CO)_2^+$	$^3\Delta_g$	+199.9	2.009 Å, 1.147 Å, 180°, 180°
$Rh(CO)_2^+$	$^3B_2$	+202.4	1.964 Å, 1.152 Å, 104.4°, 172.3°
$Ir(CO)_2$	$^2\Delta_g$	0.0	1.912 Å, 1.167 Å, 180°, 180°
$Ir(CO)_2^-$	$^1A_1$	−62.2	1.837 Å, 1.205 Å, 130.3°, 162.9°
$Ir(CO)_2^+$	$^3\Delta_g$	+208.4	1.960 Å, 1.150 Å, C:180°, 180°

(B) For $Rh(CO)_2$, $Rh(CO)_2^-$ and $Rh(CO)_2^+$ Using the BP86 and B3LYP Functionals and 6-31+G* Basis Set

		BP86		B3LYP	
molecule	state	energies	geometries (Rh−C, C−O, ∠C−Rh−C, ∠Rh−C−O)	energies	geometries
$Rh(CO)_2$	$^2B_2$	0.0	1.864 Å, 1.171 Å, 100.5°, 168.8°	+2.3	1.894 Å, 1.155 Å, 101.5°, 170.1°
$Rh(CO)_2$	$^2A_1$	+2.6	1.918 Å, 1.168 Å, 144.2°, 168.1°		converged to $^2\Delta_g$
$Rh(CO)_2$	$^2\Sigma_g$	+4.7	1.936 Å, 1.163 Å, linear	+1.5	1.955 Å, 1.148 Å, linear
$Rh(CO)_2$	$^2\Delta_g$	+6.1	1.951 Å, 1.160 Å, linear	0.0	1.968 Å, 1.146 Å, linear
$Rh(CO)_2$-	$^1A_1$	−58.8	1.852 Å, 1.197 Å, 125.8°, 161.5°	−49.8	1.859 Å, 1.182 Å, 126.9°,162.4°
$Rh(CO)_2^+$	$^3\Delta_g$	+199.8	2.018 Å, 1.143 Å, linear	+185.2	2.059 Å, 1.129 Å, linear
$Rh(CO)_2^+$	$^3B_2$	+202.9	1.973 Å, 1.147 Å, 104.5°, 172.8°	+191.9	2.047 Å, 1.131 Å, 105.4°, 175.6°

[a] Co calculation used 6-311+G* basis for C and O. Rh and Ir calculations used D95* basis.

observed for cobalt, rhodium, iron, and nickel carbonyl anions.[13,23,24] These absorptions show mixed isotopic spectra analogous to those for the rhodium counterparts (Figure 6), which determines the *x* values, but spectra are complicated by the neutral cluster absorptions. Our BP86 frequency calculations confirm these assignments, with scale factors ranging from 0.987 to 1.008. Note again the large carbon isotopic dependence for the monocarbonyl anion absorption and agreement with the solution absorption[16] for $Ir(CO)_4^-$ at 1898 cm^{-1}.

The cation region (not shown) reveals two sharp new absorptions at 2156.5 and 2153.8 cm^{-1}, and the latter increases much more than the former on annealing, particularly with CCl_4 doping, which enhances these absorptions by a factor of 3 and confirms the cation identification.[24,34] Our BP86 calculations predict 2128.2 and 2115.6 cm^{-1} harmonic modes for $IrCO^+$ and $Ir(CO)_2^+$, which are in excellent agreement with the observed values.

Models for Rhodium Catalyst Systems. These simple RhCO species can be used as an indicator of local metal charge in larger complexes, supported metal catalyst systems, and metal surfaces, since the additional electron(s) added to $RhCO^+$ to form RhCO and $RhCO^-$ are Rh−C bonding *but* C−O antibonding. Table 4 compares the decrease in calculated Rh−C and increase in calculated C−O bond lengths in the series. In addition, Mulliken charge distributions show an increase in charge on the carbonyl, which is manifested in a decrease in carbonyl vibrational frequency, as illustrated below. The present neon matrix values are expected to be within 10−30 cm^{-1} of the yet-to-be-determined gas-phase frequencies.

+0.88 +0.05 +0.07	+0.12 −0.02 −0.10	−0.73 −0.04 −0.23
$RhCO^+$	RhCO	$RhCO^-$
$\nu_{co} = 2174$ cm^{-1}	$\nu_{co} = 2022$ cm^{-1}	$\nu_{co} = 1828$ cm^{-1}

A series of catalytically active $Rh^ICl(CO)(PR_3)_2$ complexes in CH_2Cl_2 solution gives carbonyl frequencies ranging from 2016 cm^{-1} for R = OPh to 1956 cm^{-1} for R = Et.[8] This comparison suggests that the $P(OPh)_3$ ligands effectively *neutralize* the Rh center and that PEt_3 ligands transfer enough electron density to neutralize and impart a partial negative charge on the Rh center. The Rh center in the CpRh(CO) transient[7] absorbing at 1985 cm^{-1} also appears to contain a partial negative charge. The same conclusion can be reached for $CpRh(CO)_2$ and $CpIr(CO)_2$ where C−O stretching frequencies[39−41] are some 55 cm^{-1} *lower* than neon matrix frequencies for $Rh(CO)_2$ (2031 cm^{-1}) and $Ir(CO)_2$ (2014 cm^{-1}).

Our calculations for the $Rh(CO)(Cl)(PH_3)_2$ model compound (Table 11) support this conclusion; the C−O bond is *longer*, the frequency *lower*, and the Mulliken charge more *negative* than for the $(OC)_2Rh(Cl)_2Rh(CO)_2$ model compound (Table 10). It is expected that these *trends* would be more pronounced if we had been able to calculate the complex with the more electron-donating R = Et substituent.

The catalytic material $Rh^I(CO)_2$ on alumina absorbing near 2100 and 2030 cm^{-1} photodissociates to a $Rh^I(CO)$ species absorbing near 2060 cm^{-1}.[3,4] The present monocarbonyl observations provide a scale and suggest that the rhodium monocarbonyl species on alumina contains partial positive charge near +0.3, but $Rh^I(CO)$ on zeolite[6] absorbing at 2096 cm^{-1} is more positively charged near +0.5. On silica, the $Rh^I(CO)$ species has an intermediate absorption,[5] which suggests an intermediate local charge. The $RhCO^{+,0,-}$ frequencies give an almost linear relationship with charge; the $RhCO^+$ frequency in solid neon (2174 cm^{-1}) nearly matches the value for $Na^+(CO)$ on zeolite (2178 cm^{-1}),[42] which provides a calibration mark for our scale.

The bent $Rh^I(CO)_2$ species on alumina has an antisymmetric C−O frequency in agreement with linear OC−Rh−CO (2031 cm^{-1}), which is substantially lower than the observed linear cation frequency (2185 cm^{-1}) in solid neon. However, calculations for the higher energy bent ($^2B_2$) neutral predict 75 ± 15 cm^{-1} lower frequencies and for the bent ($^3B_2$) cation 40 ± 10 cm^{-1} lower frequencies than for the linear dicarbonyls. So we have bent $Rh(CO)_2^+$ and bent $Rh(CO)_2$ frequencies scaled from observed linear values as benchmarks for the $Rh^I(CO)_2$

TABLE 7: Calculated Isotopic C−O Stretching Vibrational Frequencies (cm^{-1}), Intensities (km/mol), and Isotopic Frequency Ratios

(A) For the Dicarbonyl Structures Described in Table 6A

molecule	frequency (intensity) $(^{12}C^{16}O)_2$	$(^{13}C^{16}O)_2$	$(^{12}C^{18}O)_2$	$R(^{12}C/^{13}C)$	$R(^{16}O/^{18}O)$
$Co(CO)_2^+$	2136.4 (869) (σ_u)	2088.3	2085.6	1.0230	1.0244
$^3\Delta_g$	2189.6 (0) (σ_g)	2138.6	2140.1	1.0238	1.0231
$Rh(CO)_2$	1946.8 (997) (b_2)	1901.4	1902.9	1.0239	1.0231
$^2B_2$	2000.8 (318) (a_1)	1953.0	1957.4	1.0245	1.0222
$Rh(CO)_2$	1961.4 (1423) (b_2)	1916.8	1915.5	1.0233	1.0240
$^2A_1$	2027.8 (104) (a_1)	1979.3	1983.7	1.0245	1.0222
$Rh(CO)_2$	1974.0 (1847) (σ_u)	1929.7	1926.8	1.0230	1.0245
$^2\Sigma_g^+$	2069.6 (0) (σ_g)	2019.8	2025.2	1.0247	1.0219
$Rh(CO)_2$	2004.1 (1810) (σ_u)	1958.8	1956.9	1.0231	1.0241
$^2\Delta_g$	2086.8 (0) (σ_g)	2036.7	2041.8	1.0246	1.0220
$Rh(CO)_2^-$	1813.2 (1671) (b_2)	1770.1	1773.7	1.0243	1.0223
$^1A_1$	1879.6 (374) (a_1)	1833.1	1841.1	1.0254	1.0209
$Rh(CO)_2^+$	2132.7 (646) (σ_u)	2084.8	2081.8	1.0230	1.0244
$^3\Delta_g$	2180.2 (0) (σ_g)	2129.2	2131.1	1.0240	1.0230
$Rh(CO)_2^+$	2095.1 (548) (b_2)	2047.7	2045.6	1.0231	1.0242
$^3B_2$	2124.8 (118) (a_1)	2075.9	2075.8	1.0236	1.0236
$Ir(CO)_2$	1998.0 (1853) (σ_u)	1952.3	1951.7	1.0234	1.0237
$^2\Delta_g$	2099.2 (0) (σ_g)	2047.3	2056.3	1.0254	1.0209
$Ir(CO)_2^-$	1818.9 (1604) (b_2)	1774.4	1781.2	1.0251	1.0212
$^1A_1$	1895.1 (344) (a_1)	1846.4	1859.2	1.0264	1.0193
$Ir(CO)_2^+$	2115.6 (871) (σ_u)	2067.8	2065.5	1.0231	1.0243
$^3\Delta_g$	2184.9 (0) (σ_g)	2132.4	2137.8	1.0246	1.0220

(B) For the Dicarbonyl Structures Described in Table 6B[a]

	BP86					
molecule	frequency (intensity) $(^{12}C^{16}O)_2$	$(^{13}C^{16}O)_2$	$(^{12}C^{18}O)_2$	$R(^{12}C/^{13}C)$	$R(^{16}O/^{18}O)$	B3LYP $(^{12}C^{16}O)_2$
$Rh(CO)_2$	1947.1 (1050)	1902.1	1902.8	1.0237	1.0233	2038.3 (1293)
$^2B_2$	2002.8 (317)	1955.3	1958.9	1.0243	1.0224	2095.0 (380)
$Rh(CO)_2$	1962.4 (1493)	1918.0	1916.1	1.0231	1.0242	
$^2A_1$	2028.4 (108)	1980.3	1983.9	1.0243	1.0224	
$Rh(CO)_2$	1973.9 (1929)	1929.9	1926.3	1.0228	1.0247	2069.6 (2202)
$^2\Sigma^+$	2071.3 (0)	2021.7	2026.4	1.0245	1.0222	2161.7 (0)
$Rh(CO)_2$	2006.6 (1871)	1961.5	1958.9	1.0230	1.0244	2097.7 (2054)
$^2\Delta_g$	2091.1 (0)	2041.1	2045.6	1.0245	1.0222	2179.4 (0)
$Rh(CO)_2^-$	1801.0 (1864)	1758.5	1761.3	1.0242	1.0225	1869.8 (2358)
$^1A_1$	1870.9 (429)	1825.0	1832.3	1.0252	1.0211	1948.6 (499)
$Rh(CO)_2^+$	2104.9 (547)	2057.4	2055.0	1.0231	1.0243	2229.4 (483)
$^3B_2$	2134.6 (109)	2085.7	2085.1	1.0234	1.0237	2254.2 (113)
$Rh(CO)_2^+$	2141.5 (650)	2093.6	2090.2	1.0229	1.0245	2254.7 (611)
$^3\Delta_g$	2188.5 (0)	2137.6	2138.9	1.0238	1.0232	2288.7 (0)

frequencies. On alumina, the $Rh^I(CO)_2$ frequencies are 0.3 of the way between the neutral and cation benchmarks, and on zeolites they are halfway. We suggest that on alumina the local charge on Rh in the $Rh(CO)_2$ species is near +0.3 and on zeolite near +0.5, which are the same charges deduced here for the supported monocarbonyls.

The results of BP86 calculations on the $(OC)_2Rh(Cl)_2Rh(CO)_2$ model compound for the supported $Rh(CO)_2$ species[3c,d,43,44] are of particular interest here. First, the calculated bond angles and lengths (Table 10) are in excellent agreement with X-ray values for the solid compound.[45] Second, the two strongest calculated infrared absorptions and relative intensities are in excellent agreement with the gas-phase spectrum.[46] The scale factors 1.003 and 1.013 for the two carbonyl stretching frequencies match those found here for RhCO and $Rh(CO)_2$. Third, the calculated Mulliken charges[27] provide an approximate measure of local charge on Rh in this model compound; the Mulliken charge (+0.22) on Rh is only slightly larger than calculated here for RhCO (+0.12) and is in accord with the +0.3 value deduced here from observed frequencies for the local charge on Rh in the supported $Rh(CO)_2$ species. In this regard Mulliken populations calculated for linear $^2\Delta_g$ $Rh(CO)_2$ are Rh (+0.23), C (−0.06), O (−0.05) and for the bent $^2B_2$ state are Rh (+0.24), C (−0.04), O (−0.08).

For pure metal surfaces, linearly adsorbed "top-site" CO low (0.1) monolayer coverage on Rh(100) at 90 K gives a carbonyl vibration[9] at 2013 cm^{-1}, which is near neutral RhCO at 2022 cm^{-1}. Extrapolating the infrared band for CO on Ir(111) to zero coverage[10] gives a "singleton frequency" of 2028 cm^{-1}, which is very close to IrCO in solid neon at 2024 cm^{-1}. It is interesting to note that our neutral RhCO and IrCO frequencies in solid neon are in very good agreement with linear, top-site, singleton frequencies on the metal surfaces.

Reaction Mechanisms. The neutral metal carbonyls are formed by direct reaction during matrix deposition and on annealing:

$$M + xCO \rightarrow M(CO)_x \qquad (x = 1, 2, 3, 4; M = Rh, Ir) \quad (1)$$

These reactions for $x = 1$ are spontaneous for Rh and Ir and exothermic by 42 and 75 kcal/mol, respectively, as calculated at the CASMCSCF level.[21]

TABLE 8: Calculated (BP86/ECP/D95*) Relative Energies (kcal/mol), C−O Stretching Frequencies (cm^{-1}), Intensities (km/mol), and Isotopic Frequency Ratios for the Rh and Ir Tricarbonyl Molecules, Cations, and Anions

		frequency (intensity)				
molecule	energy	$(^{12}C^{16}O)_3$	$(^{13}C^{16}O)_3$	$(^{12}C^{18}O)_3$	$R(^{12}C/^{13}C)$	$R(^{16}O/^{18}O)$
$Rh(CO)_3$,[a] $^2A_1$	0	1981.4 (1593) (b_2)	1936.6 (1503)	1934.6 (1546)	1.0231	1.0242
		1997.5 (619) (a_1)	1950.5 (585)	1953.1 (599)	1.0241	1.0227
		2053.6 (16) (a_1)	2004.8 (15)	2008.6 (16)	1.0243	1.0224
$Rh(CO)_3^-$,[b] $^1A_1'$	−62.1	1848.3 (1513) (e)	1804.9 (1437)	1807.1 (1457)	1.0240	1.0228
		1848.3 (1513) (e)	1804.9 (1437)	1807.1 (1457)	1.0240	1.0228
		1920.5 (0) (a_1)	1874.0 (98)	1879.6 (98)	1.0248	1.0218
$Rh(CO)_3^+$,[c] $^1A_1$	+179.8	2101.1 (357) (a_1)	2051.5 (334)	2054.6 (349)	1.0242	1.0226
		2114.8 (735) (b_2)	2067.4 (688)	2064.3 (721)	1.0229	1.0245
		2180.2 (4) (a_1)	2128.2 (3)	2132.6 (5)	1.0244	1.0223
$Ir(CO)_3$,[d] $^2A_1$	0	1980.6 (1585) (b_2)	1935.0 (1494)	1935.0 (1539)	1.0236	1.0236
		2005.5 (722) (a_1)	1956.9 (681)	1963.1 (701)	1.0248	1.0216
		2063.4 (9) (a_1)	2012.7 (8)	2020.5 (9)	1.0252	0.0212
$Ir(CO)_3^-$,[e] $^1A_1'$	−66.6	1857.7 (1535) (e)	1812.9 (1458)	1818.0 (1475)	1.0247	1.0218
		1857.7 (1535) (e)	1812.9 (1458)	1818.0 (1475)	1.0247	1.0218
		1936.4 (0) (a_1)	1887.9 (0)	1897.7 (0)	1.0257	1.0204
$Ir(CO)_3^+$,[f] $^1A_1$	+185.1	2104.4 (899) (b_2)	2056.9 (840)	2054.5 (885)	1.0231	1.0243
		2105.9 (435) (a_1)	2054.4 (407)	2061.8 (426)	1.0251	1.0214
		2182.5 (7) (a_1)	2129.5 (5)	2136.5 (10)	1.0249	1.0215

[a] Structure: C_{2v} symmetry. Rh−C(ax): 1.874 Å. C−O: 1.170 Å. Rh−C(eq): 1.952 Å. C−O: 1.167 Å. $\angle C_{eq}RhC_{eq}$: 164.0°. [b] Structure: D_{3h} symmetry. Rh−C: 1.905 Å. C−O: 1.192 Å. [c] Structure: C_{2v} symmetry. Rh−C(ax): 1.836 Å. C−O: 1.157 Å. Rh−C(eq): 1.972 Å. C−O: 1.149 Å. $\angle C_{eq}RhC_{eq}$: 179.1°. [d] Structure: C_{2v} symmetry. Ir−C(ax): 1.854 Å. C−O: 1.173 Å. Ir−C(eq): 1.925 Å. C−O: 1.170 Å. $\angle C_{eq}IrC_{eq}$: 160.9°. [e] Structure: D_{3h} symmetry. Ir−C: 1.888 Å. C−O: 1.195 Å. [f] Structure: C_{2v} symmetry. Ir−C(ax): 1.820 Å. C−O: 1.160 Å. Ir−C(eq): 1.960 Å. C−O: 1.151 Å. $\angle C_{eq}IrC_{eq}$: 177.8°.

TABLE 9: Calculated (BP86/ECP/D95*) Relative Energies (kcal/mol), C−O Stretching Frequencies (cm^{-1}), Intensities (km/mol), and Isotopic Frequency Ratios for the Rh and Ir Tetracarbonyl Molecules, Anions, and Cations

		frequency (intensity)				
molecule	energy	$(^{12}C^{16}O)_4$	$(^{13}C^{16}O)_4$	$(^{12}C^{18}O)_4$	$R(^{12}C/^{13}C)$	$R(^{16}O/^{18}O)$
$Rh(CO)_4$,[a] $^2B_2$	0	1988.0 (1308) (e)	1942.7 (1238)	1941.5 (1263)	1.0233	1.0240
		1995.7 (298) (b_2)	1949.1 (281)	1950.8 (289)	1.0239	1.0230
		2061.2 (0) (a_1)	2012.5 (0)	2015.6 (0)	1.0242	1.0226
$^2A_1$[b]	+5.3	1992.7 (983) (e)	1947.3 (932)	1946.1 (948)	1.0233	1.0239
		2000.4 (587) (a_1)	1954.0 (556)	1955.0 (566)	1.0237	1.0232
		2054.7 (24) (a_1)	2006.5 (22)	2008.6 (24)	1.0240	1.030
$Rh(CO)_4^-$,[c] $^1A_1$	−68.7	1882.7 (1223) (t_2)	1838.6 (1165)	1840.5 (1171)	1.0240	1.0229
		1953.6 (0) (a_1)	1906.9 (0)	1911.2 (0)	1.0245	1.0222
$Rh(CO)_4^+$,[d] ^1A_g	+161.6	2115.2 (812) (e_u)	2067.6 (760)	2064.9 (797)	1.0230	1.0244
		2146.4 (0) (a_{2u})	2096.2 (0)	2098.2 (0)	1.0239	1.0230
		2193.8 (0) (a_{1g})	2141.4 (0)	2146.1 (0)	1.0245	1.0222
$Ir(CO)_4$,[e] $^2B_2$	0	1988.6 (1333) (e)	1942.4 (1261)	1943.5 (1288)	1.0238	1.0232
		2002.0 (325) (b_2)	1953.8 (307)	1959.0 (315)	1.0247	1.0219
		2074.0 (0) (a_1)	2023.3 (0)	2030.6 (0)	1.0251	1.0214
$Ir(CO)_4$,[f] $^2A_1$	+7.6	1985.2 (1008) (e)	1939.1 (955)	1940.2 (972)	1.0238	1.0232
		2000.9 (652) (a_1)	1953.4 (617)	1957.1 (629)	1.0243	1.0224
		2055.7 (45) (a_1)	2006.2 (42)	2011.7 (45)	1.0247	1.0219
$Ir(CO)_4^-$,[g] $^1A_1$	−71.4	1886.3 (1218) (t_2)	1841.0 (1160)	1845.7 (1165)	1.0246	1.0220
		1959.9 (0) (a_1)	1911.6 (0)	1919.4 (0)	1.0253	1.0211
$Ir(CO)_4^+$,[h] ^1A_g	+165.2	2109.1 (973) (e_u)	2061.4 (910)	2059.4 (957)	1.0231	1.0241
		2147.8 (0) (a_{2u})	2096.8 (0)	2100.8 (0)	1.0243	1.0224
		2201.1 (0) (a_{1g})	2147.6 (0)	2154.7 (0)	1.0249	1.0215

[a] Structure: D_{2d} symmetry. Rh−C: 1.951 Å. C−O: 1.168 Å. ∠CRhC: 145.1°. [b] Structure: C_{3v} symmetry. Rh−C(ax): 1.907 Å. C−O: 1.168 Å. Rh−C(eq): 1.984 Å. C−O: 1.167 Å. $C_{ax}RhC_{eq}$: 97.5°. $\angle C_{eq}RhC_{eq}$: 118.3°. [c] Structure: T_d symmetry. Rh−C: 1.935 Å. C−O: 1.186 Å. [d] Structure: D_{4h} symmetry. Rh−C: 1.967 Å. C−O: 1.150 Å. [e] Structure: D_{2d} symmetry. Ir−C: 1.926 Å. C−O: 1.171 Å. ∠CIrC: 145.5°. [f] Structure: C_{3v} symmetry. Ir−C(ax): 1.893 Å. C−O: 1.170 Å. Ir−C(eq): 1.945 Å. C−O: 1.170 Å. $\angle C_{ax}IrC_{eq}$: 98.7°. $\angle C_{eq}IrC_{eq}$: 117.7°. [g] Structure: T_d symmetry. Ir−C: 1.911 Å. C−O: 1.190 Å. [h] Structure: D_{4h} symmetry. Ir−C: 1.957 Å. C−O: 1.151 Å.

The anions are formed by electron capture and the addition of more CO ligands during deposition and on annealing:

$$MCO(^2\Delta) + e^- \rightarrow MCO^-(^1\Sigma^+) \qquad (M = Rh, Ir) \quad (2a)$$

$$MCO^- + (x-1)CO \rightarrow M(CO)_x^- \qquad (x = 2, 3, 4) \quad (2b)$$

$$M(CO)_x + e^- \rightarrow M(CO)_x \qquad (x = 2, 3, 4) \quad (2c)$$

Reaction 2a is exothermic by −35 and −36 kcal/mol, respectively, for Rh and Ir (Table 4). Although these energies are approximate, such a calculation for FeCO is within 4% of the experimental electron affinity (26.7 kcal/mol).[24,47] Clearly, RhCO an IrCO have greater electron affinities than FeCO. On the basis of the need for higher energy photons to bleach anions with increasing x values, the exothermicities of reaction 2c increase with increasing x, as found for $Fe(CO)_x$ and $Ni(CO)_x$. The calculated energy differences of neutral minus anion increase with x; for $x = 2$, it is −62, −62 for Rh, Ir, for $x = 3$, it is −62, −67 for Rh, Ir, and for $x = 4$, it is −74, −71 kcal/

TABLE 10: Calculated (BP86/ECP/D95*) and Observed Parameters for the $(OC)_2Rh(Cl)_2Rh(CO)_2$ Molecule

	observed[a]	BP86	Mulliken charge
C−O	1.14, 1.21 Å	1.167 Å	O (−0.06)
Rh−C	1.77, 1.85 Å	1.853 Å	C (−0.02)
Rh−Cl	2.33, 2.38 Å	2.445 Å	Rh (+0.22)
Cl···Cl	(3.2 Å)	3.282 Å	Cl (−0.14)
Rh···Rh	3.12 Å	3.193 Å	
∠C−Rh−C	91°	91.3°	
dihedral ∠(Rh−$(Cl)_2$−Rh)	124°	124.8°	
ν(C−O), b_2	2095 cm^{-1}	2068 (1069)[b]	
ν(C−O), b_1	2033 cm^{-1}	2018 (1265)[b]	

[a] Distances and angles are obtained from X-ray measurements of the solid (from ref 45). Frequencies are obtained for the gas phase (from ref 46). Molecule has C_{2v} symmetry. [b] Intensities (km/mol) in parentheses.

TABLE 11: Calculated (BP86/ECP/D95*) Parameters for the $Rh(CO)(Cl)(PH_3)_2$ Complex[a]

	bond length and angle	Mulliken charge
C−O	1.178 Å	O (−0.12)
Rh−C	1.838 Å	C (+0.03)
Rh−Cl	2.400 Å	Rh (−0.01)
Rh−P	2.318 Å	Cl (−0.34)
∠C−Rh−Cl	180°	P (−0.26)
∠P−Rh−P	169°	3H (+0.48)

[a] C−O stretching frequency, 1983 cm^{-1}. Rh−C stretching frequency, 547 cm^{-1}.

mol for Rh, Ir. Clearly, the $M(CO)_x$ radicals have considerable electron affinities, and the high electron affinity of both $M(CO)_4$ species is attested by the stability of these $M(CO)_4^-$ anions in solution.[14−16] These energy differences provide electron affinity estimates[48] until gas-phase measurements can be made. Comparable matrix photolysis for these $M(CO)_4^-$ anions suggests electron affinities at least as large as that measured for $Co(CO)_4^-$ ($\geq$2.35 eV)[49] and for $Fe(CO)_4^-$ (2.4 eV).[47]

The cations are formed by reactions 3a and 3b during deposition and on annealing:

$$M^+ + CO \rightarrow MCO^+ \qquad (M = Rh, Ir) \qquad (3a)$$

$$MCO^+ + (x-1)CO \rightarrow M(CO)_x^+ \qquad (x = 2, 3, 4) \qquad (3b)$$

Addition of trace CCl_4 to these samples captures the electrons that might undergo reactions 2a and 2c, thus severely limiting anion formation, and the electrons that could neutralize metal cations, thereby enhancing reactions 3a and 3b. This chemical electron-trapping effect has been observed in argon matrix studies of the Co, Ni, and Fe carbonyl systems.[13,23,24,34]

Conclusions

Laser-ablated Co, Rh, and Ir atoms react with CO during condensation in excess neon to form the $M(CO)_x$ radical species. For Co, the spectra are in excellent agreement with thermal atom experiments,[11] but for Rh and Ir, which require higher evaporation temperatures, laser ablation reduces the heat load on the matrix and enables better product matrix isolation and identification of intermediate carbonyl species than pervious thermal atom investigations.[12] The neon matrix also proves to be an advantage for product resolution. Laser ablation also provides metal cations and electrons and has made possible the first vibrational spectroscopic investigation of Co, Rh, and Ir carbonyl cations and anions with isotopic substitution.

The Co, Rh, Ir comparisons in a common carbonyl species show an increase in carbonyl frequency from Co to Rh for all species, since the larger Rh 4d orbitals are less effective at backbonding than the smaller Co 3d orbitals. However, from Rh to Ir the carbonyl frequencies both increase and decrease, so there is no clear trend; carbonyl frequencies are compared in Table 12 for the Co, Rh, Ir transition metal family.

TABLE 12: Neon Matrix Frequencies (cm^{-1}) for Co, Rh, and Ir Carbonyl Cations, Molecules, and Anions

carbonyl	Co	Rh	Ir
$M(CO)_4^+$		2162	
$M(CO)_3^+$		2168	
$M(CO)_2^+$	2169	2185	2154
MCO^+	2166	2174	2157
$M(CO)_4$	2030, 2022[a]	2019[b]	2011[b]
$M(CO)_3$	1992[c]	2029, 2020[d]	2021, 2012[d]
$M(CO)_2$	1946	2031[e]	2015[e]
MCO	1974	2023	2025
$M(CO)_4^-$	1895	1906	1902
$M(CO)_3^-$	1829	1865	1860
$M(CO)_2^-$	1847, 1789[f]	1900, 1817[f]	1818[f]
MCO^-	1820	1829	1843

[a] C_{3v} structure. [b] D_{2d} structure. [c] D_{3h} structure. [d] C_{2v} structure. [e] Linear. [f] Bent.

TABLE 13: Scale Factors (Observed[a]/Calculated[b] Frequencies) for $Co(CO)_x$, $Rh(CO)_x$, and $Ir(CO)_x$ (x = 1, 2, 3, 4) Carbonyls, Anions, and Cations

	$x=1$	$x=2$	$x=3$	$x=4$
$Co(CO)_x$	0.997	0.986	1.004	1.012
anion	0.991	1.003	1.000	1.010
cation	1.009	1.015		
$Rh(CO)_x$	1.009	1.013	1.020	1.015
anion	0.992	1.002	1.009	1.013
cation	1.021	1.024	1.032	1.022
$Ir(CO)_x$	1.001	1.008	1.016	1.011
anion	0.987	0.998	1.002	1.008
cation	1.013	1.018		

[a] Neon matrix frequencies, this work. [b] Gaussian 94, BP86 functional. $Co(CO)_{1,2,3}$ calculations from ref 13 using 6-311+G* basis set for C and O and Wachters−Hay set from Gaussian 94 for Co. The $Co(CO)_4$ calculation using ADF (Ryeng, H.; Gropen, O.; Swang, O. *J. Phys. Chem. A* **1997**, *101*, 8956) is probably within 10 cm^{-1} of a BP86 value. $Rh(CO)_x$ and $Ir(CO)_x$ calculations (this work) were done using D95* for C and O and LanL ECP plus DZ for Rh and Ir.

Density functional theory using effective core potentials for Rh and Ir metals has been employed to help identify these molecules, cations, and anions, and the experimental observations provide a test for this application of theory. Table 13 compares the scale factors (observed/calculated) for the C−O stretching modes of the Co, Rh, and Ir carbonyl species observed here using the BP86 functional. Most of the calculated carbonyl stretching frequencies are *within* 1%, which is excellent systematic agreement; the $Rh(CO)_x^+$ cation calculations are 2−3% too high. Calculations using the B3LYP functional gave frequencies 3% too high for $^2\Delta$ RhCO[17] and $^2\Delta_g$ $Rh(CO)_2$ species. Carbonyl frequencies for the model compound $(OC)_2Rh(Cl)_2Rh(CO)_2$ are calculated with the same precision (1% high) at the BP86 level of theory. Finally, similar DFT calculations[50] for rhodium oxides using the same basis set produce lower scale factors (0.94, 0.95) for the Rh−O modes in RhO and ORhO. Clearly, a *theoretical* description of the Rh−O bond is a more difficult problem than for the C−O bond in rhodium carbonyls.

The observed and calculated $^{12}C/^{13}C$ and $^{16}O/^{18}O$ isotopic frequency ratios provide a measure of the normal vibrational mode, and excellent agreement is found between experiment and theory. In the $RhCO^+$, RhCO, $RhCO^-$ series the added electron(s) are metal−carbon bonding but carbon−oxygen antibonding and the Rh−C bond lengths decrease while the

C−O bond lengths increase (Table 4). The observed and calculated $^{12}C/^{13}C$ ratios *increase* while the $^{16}O/^{18}O$ ratios *decrease* in this series, which measure the increased carbon participation in the normal mode by coupling with the metal through the Rh−C bond. Agreement between observed and calculated ^{13}CO shifts in this monocarbonyl series is within 1.4 cm^{-1} out of 45.9 cm^{-1}, 1.9 cm^{-1} out of 47.4 cm^{-1}, and 1.8 cm^{-1} out of 49.1 cm^{-1}, respectively, which confirms these normal mode descriptions and vibrational assignments.

Our neon matrix characterization of the simple $RhCO^+$, RhCO, $RhCO^-$ and $Rh(CO)_2^+$, $Rh(CO)_2$, $Rh(CO)_2^-$ species over a 350 cm^{-1} range provides almost linear frequency scales[51] for comparison of catalytically active Rh carbonyl complexes to estimate charge on the metal centers. Previous studies of CO molecular probes of metal charge on zeolites have revealed blue-shift displacements of the C−O frequency for CO bound to metal cation sites,[42] and studies of CO on supported silica find 70−90 cm^{-1} blue shifts[52] on changing the oxidation state from Cu^+ to Cu^{2+}. Such "nonclassical" carbonyls with frequencies higher than CO itself have been explained by electrostatic effects.[53] The C−O frequencies associated with divalent transition metal cations on silica are in the 2170−2210 cm^{-1} range,[52] only slightly higher than our $RhCO^+$ band at 2174 cm^{-1}; this suggests that the local charge for these "divalent" transition metal cations on silica is slightly higher than +1.0 but not nearly as high as +2.0.

Finally, the observation of CO^+ at 2194.3 cm^{-1} in these experiments shows that the laser ablation process provides vacuum ultraviolet radiation in excess of the 14.0 eV ionization energy of CO.[54]

Acknowledgment. We gratefully acknowledge NSF support for this research under Grant CHE 97-00116 and S. P. Willson for performing the argon matrix experiments with rhodium.

References and Notes

(1) Parshall, G. W.; Ittel, S. D. *Homogeneous Catalysis*; Wiley-Interscience: New York, 1992.

(2) (a) Falbe, J. *Carbon Monoxide in Organic Synthesis*; Springer-Verlag: Berlin, 1980. (b) van Rooy, A.; de Bruijn, J. N. H.; Roobek, K. F.; Kramer, P. C. J.; Van Leeuwen, P. W. N. M. *J. Organomet. Chem.* **1996**, *507*, 69 and references therein.

(3) (a) Garland, C. W.; Lord, R. C.; Troiano, P. F. *J. Phys. Chem.* **1965**, *69*, 1188. (b) Cavanagh, R. R.; Yates, J. T., Jr. *J. Chem. Phys.* **1981**, *74*, 4150. (c) Yates, J. T., Jr.; Kolasinski, K. *J. Chem. Phys.* **1983**, *79*, 1026. (d) Paul, D. P.; Ballinger. T. H.; Yates, J. T., Jr. *J. Phys. Chem.* **1990**, *94*, 4617.

(4) (a) Ballinger, T. H.; Yates, J. T., Jr. *J. Am. Chem. Soc.* **1992**, *114*, 10074. (b) Wovchko, E. A.; Yates, J. T., Jr. *J. Am. Chem. Soc.* **1996**, *118*, 10250. (c) Wovchko, E. A.; Yates, J. T., Jr. *J. Am. Chem. Soc.* **1998**, *120*, 7544.

(5) (a) Basu, P.; Panayotov, D.; Yates, J. T., Jr. *J. Am. Chem. Soc.* **1988**, *110*, 2074. (b) Fisher, I. A.; Bell, A. T. *J. Catal.* **1996**, *162*, 54. (c) Anderson, J. A.; Rochester, C. H.; Wang, Z. J. *J. Mol. Catal. A* **1999**, *139*, 285.

(6) Miessner, H. *J. Am. Chem. Soc.* **1994**, *116*, 11522.

(7) (a) Wasserman, E. P.; Moore, C. B.; Bergman, R. G. *Science* **1992**, *255*, 315. (b) Schultz, R. H.; Bengali, A. A.; Tauber, M. J. *J. Am. Chem. Soc.* **1994**, *116*, 7369. (c) Bengali, A. A.; Schultz, R. H.; Moore, C. B. *J. Am. Chem. Soc.* **1994**, *116*, 9585.

(8) Serron, S.; Nolan, S. P.; Moloy, K. G. *Organometallics* **1996**, *15*, 4301 and references therein.

(9) Leung, L.-W.; He, J.-W.; Goodman, D. W. *J. Chem. Phys.* **1990**, *93*, 8328.

(10) Lauterbach, J.; Boyle, R. W.; Schick, M.; Mitchell, W. J.; Meng, F.; Weinberg, W. H. *Surf. Sci.* **1996**, *350*, 32 and references therein.

(11) Hanlan, L. A.; Huber, H.; Kundig, E. P.; McGarvey, B. R.; Ozin, G. A. *J. Am. Chem. Soc.* **1975**, *97*, 7054.

(12) Ozin, G. A.; Hanlan, A. J. L. *Inorg. Chem.* **1979**, *18*, 2091.

(13) Zhou, M. F.; Andrews, L. *J. Phys Chem. A* **1998**, *102*, 10250. The $CoCO^-$ state is $^3\Delta$.

(14) Edgell, W. F.; Lyford, J.; Barbetta, A.; Jose, C. I. *J. Am. Chem. Soc.* **1971**, *93*, 6403.

(15) Chini, P.; Martinengo, S. *Inorg. Chim. Acta* **1969**, *3*, 21.

(16) Malatesta, L.; Caglio, G.; Angoletta, M. *Chem. Commun.* **1970**, 532.

(17) McKee, M. L.; Worley, S. D. *J. Phys. Chem.* **1988**, *92*, 3699; *J. Phys. Chem. A* **1997**, *101*, 5600.

(18) Barnes, L. A.; Rosi, M.; Bauschlicher, C. W., Jr. *J. Chem. Phys.* **1990**, *93*, 609.

(19) Mains, G. J.; White, J. M. *J. Phys. Chem.* **1991**, *95*, 112.

(20) Papai, I.; Goursot, A.; St. Amant, A.; Salahub, D. R. *Theor. Chim. Acta* **1992**, *84*, 217.

(21) Dai, D.; Balasubramanian, K. *J. Chem. Phys.* **1994**, *101*, 2148.

(22) Burkholder, T. R.; Andrews, L. *J. Chem. Phys.* **1991**, *95*, 8697. Hassanzadeh, P.; Andrews, L. *J. Phys. Chem.* **1992**, *96*, 9177.

(23) Zhou, M. F.; Andrews, L. *J. Am. Chem. Soc.* **1998**, *120*, 11499.

(24) Zhou, M. F.; Chertihin, G. V.; Andrews, L. *J. Chem. Phys.* **1998**, *109*, 10893.

(25) Thompson, W. E.; Jacox, M. E. *J. Chem. Phys.* **1991**, *95*, 735.

(26) Zhou, M. F.; Andrews, L. *J. Phys. Chem. A* **1999**, *103*, 2964.

(27) Frisch, M. J.; Trucks, G. W.; Schlegel, H. B.; Gill, P. M. W.; Johnson, B. G.; Robb, M. A.; Cheeseman, J. R.; Keith, T.; Petersson, G. A.; Montgomery, J. A.; Raghavachari, K.; Al-Laham, M. A.; Zakrzewski, V. G.; Ortiz, J. V.; Foresman, J. B.; Cioslowski, J.; Stefanov, B. B.; Nanayakkara, A.; Challacombe, M.; Peng, C. Y.; Ayala, P. Y.; Chen, W.; Wong, M. W.; Andres, J. L.; Replogle, E. S.; Gomperts, R.; Martin, R. L.; Fox, D. J.; Binkley, J. S.; Defrees, D. J.; Baker, J.; Stewart, J. P.; Head-Gordon, M.; Gonzalez, C.; Pople, J. A. *Gaussian 94*, revision B.1; Gaussian, Inc.: Pittsburgh, PA, 1995.

(28) Perdew, J. P. *Phys. Rev. B* **1986**, *33*, 8822. Becke, A. D. *J. Chem. Phys.* **1993**, *98*, 5648.

(29) Lee, C.; Yang, E.; Parr, R. G. *Phys. Rev. B* **1988**, *37*, 785.

(30) Dunning, T. H., Jr.; Hay, P. J. *Modern Theoretical Chemistry*; Schaefer, H. F., III, Ed.; Plenum: NewYork, 1976.

(31) McLean, A. D.; Chandler, G. S. *J. Chem. Phys.* **1980**, *72*, 5639. Krishnan, R.; Binkley, J. S.; Seegar, R.; Pople, J. A. *J. Chem. Phys.* **1980**, *72*, 650.

(32) Hay, P. J.; Wadt, W. R. *J. Chem. Phys.* **1985**, *82*, 299.

(33) Ryeng, H.; Gropen, O.; Swang, O. *J. Phys. Chem. A* **1997**, *101*, 8956.

(34) Zhou, M. F.; Andrews, L. *J. Chem. Phys.* **1999**, *110*, 10370.

(35) Castro, M.; Salahub, D. R.; Fournier, R. *J. Chem. Phys.* **1994**, *100*, 8233.

(36) Ricca, A.; Bauschlicher, C. W., Jr. *J. Phys. Chem.* **1995**, *99*, 5922. Ricca, A.; Bauschlicher, C. W., Jr. *J. Phys. Chem.* **1994**, *98*, 12899.

(37) Bytheway, I.; Wong, M. W. *Chem. Phys. Lett.* **1998**, *282*, 219.

(38) Darling, J. H.; Ogden, J. S. *J. Chem. Soc., Dalton Trans.* **1972**, 2496.

(39) Hoyano, J. K.; Graham, W. A. G. *J. Am. Chem. Soc.* **1982**, *104*, 3723.

(40) Rest, A. J.; Whitwell, I.; Graham, W. A. G.; Hoyano, J. K.; McMaster, A. D. *J. Chem. Soc., Dalton Trans.* **1987**, 1181.

(41) Belt, S. T.; Grevels, F. W.; Klotzbücher, W. E.; McCamley, A.; Perutz, R. N. *J. Am. Chem. Soc.* **1989**, *111*, 8373.

(42) Zecchina, A.; Areán, C. O. *Chem. Soc. Rev.* **1996**, *25*, 187.

(43) van't Blik, H. F. J.; van Zon, J. B. A. D.; Huizinga, T.; Vis, J. C.; Koningsberger, D. C.; Prins, R. *J. Am. Chem. Soc.* **1985**, *107*, 3139.

(44) Wovchko, E. A.; Zubkov, T. S.; Yates, J. T., Jr. *J. Phys. Chem. B* **1998**, *102*, 10535. Zubkov, T. S.; Wovchko, E. A.; Yates, J. T., Jr. *J. Phys. Chem.* **1999**, *103*, 4845.

(45) Dahl, L. F.; Martell, C.; Wampler, D. L. *J. Am. Chem. Soc.* **1961**, *83*, 1761.

(46) Garland, C. W.; Wilt, J. R. *J. Chem. Phys.* **1962**, *36*, 1094.

(47) Engelking, P. C.; Lineberger, W. C. *J. Am. Chem. Soc.* **1979**, *101*, 5569.

(48) Gailbraith, J. M.; Schaeffer, H. F., III *J. Chem. Phys.* **1996**, *105*, 862.

(49) Simoes, J. A. M.; Beauchamp, J. L. *Chem. Rev.* **1990**, *90*, 629.

(50) Citra, A.; Andrews, L. *J. Phys. Chem. A* **1999**, *103*, 4845.

(51) Zhou, M. F.; Andrews, L. *J. Am. Chem. Soc.*, in press.

(52) Lindblad, T.; Rebenstorf, B. *Acta Chem. Scand.* **1991**, *45*, 342.

(53) Goldman, A. S.; Krogh-Jespersen, K. *J. Am. Chem. Soc.* **1996**, *118*, 12159.

(54) Hotof, H.; Niehaus, A. *Int. J. Mass Spectrom. Ion Phys.* **1970**, *5*, 415.